



POLITECNICO
MILANO 1863

SCUOLA DI INGEGNERIA INDUSTRIALE
E DELL'INFORMAZIONE



Simulation of a LEO orbiting microsat on Simulink

MSc IN SPACE ENGINEERING

Authors:

10723712	MARCELLO PARESCHI	(BSc AEROSPACE ENGINEERING - POLITECNICO DI MILANO)
10836125	DANIELE PATERNOSTER	(BSc AEROSPACE ENGINEERING - POLITECNICO DI MILANO)
10711624	ALEX CRISTIAN TURCU	(BSc AEROSPACE ENGINEERING - POLITECNICO DI MILANO)
10884250	TAMIM HARUN OR	(BSc AEROSPACE ENGINEERING - INTERNATIONAL ISLAMIC UNIVERSITY MALAYSIA)

Professor: FRANCO BERNELLI ZAZZERA

Academic year: 2023-2024

Abstract

The presented report discusses the attitude dynamics and control of a microsatellite in Sun-synchronous low-Earth orbit. The mission of the satellite is to point the Earth, due to the payload requirement. The simulation was carried out in Simulink environment. The rotational dynamics was modeled through the Euler equations, the kinematics was parametrized through two sets of Euler angles (312 - 313). The environment disturbances considered were magnetic field interaction and gravity gradient torque, as they resulted to be the most relevant after a general analysis of all the four main disturbances (SRP, air drag, magnetic, gravity gradient). The orbital motion was modeled as a restricted two-body problem.

The on-board sensors are a horizon sensor, a magnetometer and a Sun sensor. They were all modeled in Simulink taking as reference some real sensors. The actuators installed on the satellite are a magnetorquer and two reaction wheels, modeled referring to some real counterparts as well.

The control logic implemented on-board considers two algorithms. The first one deals with the de-tumbling of the spacecraft using the B-dot control, and continues until a certain condition on the value of the derivative of \mathbf{B} is satisfied. The second contemplates the slew and tracking manoeuvres together. This last phase is performed through an extension of the PD controller for non-linear dynamics.

Contents

Abstract	I
Contents	II
1 Symbols	III
1.3 Framework analysis	III
1.4 Dynamics	III
1.5 Kinematics	III
1.6 Disturbances analysis	III
1.7 Sensors	III
1.8 Attitude determination	III
1.9 Actuators	IV
1.10 Control logic	IV
1.11 Simulation results	IV
2 Requirements	IV
3 Framework Analysis	1
3.1 Satellite characterization	1
3.2 Orbit characterization	1
4 Dynamics	2
5 Kinematics	3
6 Disturbances analysis	4
6.1 Magnetic Disturbance	4
6.2 SRP Disturbance	4
6.3 Drag Disturbance	5
6.4 Gravity Gradient Disturbance	5
6.5 Simulation of all disturbances	6
7 Sensors	6
7.1 Horizon Sensor	6
7.2 Magnetometer	7
7.3 Sun Sensor	8
8 Attitude determination	8
9 Actuators	10
9.1 Magnetorquers	10
9.2 Reaction Wheels	10
10 Control logic	11
10.1 De-tumbling phase: the B-dot control	11
10.2 Slew and Nadir pointing phases	12
10.2.1 Control law for the Slew and Tracking Manoeuvre	12
10.2.2 Actuators' command logic for Slew and Nadir pointing	13
11 Simulation results	15
11.1 Detumbling analysis	15
11.2 Slew and tracking phase analysis	16
11.3 Control action analysis	17
Bibliography	19

1. Symbols

1.3. Framework analysis

I	$[kg/m^2]$	inertia matrix of S/C
a	$[km]$	semi-major axis
e	$[-]$	eccentricity
i	$[deg]$	inclination
ω	$[deg]$	pericentre anomaly
Ω	$[deg]$	RAAN
θ	$[rad]$	true anomaly
n	$[rad/s]$	mean anomaly
\mathcal{P}	$[-]$	perifocal frame
\mathcal{N}	$[-]$	inertial frame
A_{PN}	$[-]$	rotation matrix from inertial to perifocal frame
r_P	$[km]$	S/C position in \mathcal{P} frame
r_N	$[km]$	S/C position in \mathcal{N} frame

1.4. Dynamics

\mathcal{B}	$[-]$	body frame
x_b	$[-]$	x direction in \mathcal{B} frame
y_b	$[-]$	y direction in \mathcal{B} frame
z_b	$[-]$	z direction in \mathcal{B} frame
ω	$[rad/s]$	angular velocity in \mathcal{B} frame
$\dot{\omega}$	$[rad/s^2]$	angular velocity rate in \mathcal{B} frame
M_d	$[Nm]$	disturbances torque
M_c	$[Nm]$	control torque

1.5. Kinematics

s	$[rad]$	set of Euler angles
\dot{s}	$[rad/s]$	set of Euler angle's rates
312	$[-]$	sequence of axis' rotation
313	$[-]$	sequence of axis' rotation
ϕ	$[rad]$	first rotation angle
θ	$[rad]$	second rotation angle
ψ	$[rad]$	third rotation angle
A_{BN}	$[-]$	attitude matrix
tol	$[-]$	tolerance value for singularity check

1.6. Disturbances analysis

M	$[Nm]$	disturbance torque
D	$[Am^2]$	magnetic dipole from coils or parasitic currents
B	$[T]$	magnetic field vector
V	$[Tm]$	magnetic field scalar potential
ECEF	$[-]$	Earth-Centered Earth-Fixed frame
a	$[km]$	Earth's equatorial radius
r	$[km]$	radial distance from Earth's centre to S/C position (ECEF)
θ	$[rad]$	longitude (ECEF)
ϕ	$[rad]$	co-latitude (ECEF)
$p^{n,m}(\cos \theta)$	$[-]$	Gauss normalized associated Legendre functions
$g^{n,m}(t)$	$[nT]$	Schmidt semi-normalized spherical harmonic coefficients

$h^{n,m}(t)$	$[nT]$	Schmidt semi-normalized spherical harmonic coefficients
F_i	$[N]$	disturbance force acting on i-th panel
P	$[Pa]$	Sun's radiation pressure
A_i	$[m^2]$	area of i-th panel
\hat{S}_B	$[-]$	Sun's direction in \mathcal{B} frame
$\hat{N}_{B,i}$	$[-]$	i-th panel's normal direction in \mathcal{B} frame
ρ_s	$[-]$	coefficient of specular reflection
ρ_a	$[-]$	coefficient of absorption
ρ_d	$[-]$	coefficient of diffusion
ϵ	$[deg]$	obliquity of Earth
C_D	$[-]$	coefficient of drag
r_i	$[m]$	position of centre of action of the force
$v_{B,i}$	$[m/s]$	relative velocity in \mathcal{B} frame of the i-th panel
$\hat{v}_{B,i}$	$[-]$	direction of relative velocity in \mathcal{B} frame of the i-th panel
ρ	$[kg/m^3]$	density of air
ρ_0	$[kg/m^3]$	reference density of air from US Standard Atmosphere model (1976)
h_0	$[km]$	reference height from US Standard Atmosphere model (1976)
H	$[km]$	scaling height from US Standard Atmosphere model (1976)
G	$[m^3 kg^{-1} s^{-2}]$	universal gravitational constant
m_t	$[kg]$	mass of Earth
c_i	$[-]$	direction cosines of the radial direction in \mathcal{B} frame

1.7. Sensors

Np	$[rad^2 s]$	noise power
T_s	$[s]$	sampling time
σ^2	$[rad^2]$	variance of the measurment
$N.S.D.$	$[nT/\sqrt{Hz}]$	noise spectral density
I	$[A]$	intensity of current
α	$[A/W]$	coefficient of the Sun sensor
S	$[m^2]$	sensor surface area
W	$[W/m^2]$	intensity of incident radiation
θ	$[rad]$	angle of incident light

1.8. Attitude determination

J	$[-]$	cost function
α_i	$[-]$	weight of i-th sensor for J function
s_i	$[-]$	unit vector measured by i-th sensor in \mathcal{B} frame
v_i	$[-]$	unit vector calculated by on-board model in \mathcal{N} frame

ϕ	[rad]	error angle between true and measured direction without bias
$E[\phi]$	[rad]	expected value of error angle
σ_ϕ^2	[rad ²]	variance of error angle
σ_ϕ	[rad]	standard deviation of error angle

1.9. Actuators

D	[Am ²]	magnetic dipole from magnetorquers
M	[Nm]	control torque
h	[kgm ² /s]	angular momentum of reaction wheels + satellite
h_r	[kgm ² /s]	relative angular momentum of reaction wheel
\dot{h}_r	[kgm ² /s ²]	relative angular momentum rate of reaction wheel
ω_{max}	[RPM]	saturation speed of reaction wheel
\dot{h}_{max}	[Nm]	maximum available torque for reaction wheel
ω_r	[rad/s]	relative angular velocity of reaction wheel
$\dot{\omega}_r$	[rad/s ²]	relative angular velocity rate of reaction wheel
σ_ω	[RPM]	standard deviation on ω_r

1.10. Control logic

B_B	[T]	magnetic field in B frame
\dot{B}_B	[1/s]	unit vector velocity of magnetic field in B frame
k_ω	[kg · m ² /s]	gain for detumbling phase
\dot{A}_{BN}	[1/s]	rate of attitude matrix
B_N	[T]	magnetic field in N frame

\dot{B}_N	[T/s]	magnetic field rate in N frame
\mathcal{LVCH}	[−]	local vertical local horizontal frame
A_{BL}	[−]	error matrix between B and \mathcal{LVCH} frame
ξ	[deg]	angle between orbital plane and magnetic equator
ϵ	[−]	attitude error for non-linear control
ω_{BL}	[rad/s]	angular velocity error between \mathcal{LVCH} and B frames
k_1	[kg · m ² /s ²]	gain on attitude error for non-linear control
k_2	[kg · m ² /s]	gain on angular velocity error for non-linear control
α	[rad]	small Euler angles between B and \mathcal{LVCH} frame
$\dot{\alpha}$	[rad/s]	small Euler angles rate between B and \mathcal{LVCH} frame
K_p	[kg · m ² /s ²]	gain matrix on α for linear control
K_d	[kg · m ² /s]	gain matrix on $\dot{\alpha}$ for linear control
K_x	[−]	yaw inertial coefficient
K_y	[−]	roll inertial coefficient
p_{open}	[1/s]	open-loop poles for the dynamic system
p	[1/s]	closed-loop poles for the dynamic system

1.11. Simulation results

B_m	[T]	measured magnetic field
$\ \dot{B}_m\ $	[1/s]	norm of rate of change of direction of B_m
ω_{estim}	[rad/s]	on-board estimation of angular velocity

2. Requirements

	Assigned specification	Modifications	Motivation for modifications
Platform	Microsat	-	-
Attitude parameters	Euler angles	-	-
Sensor	Earth Horizon	Magnetic, Sun	Magnetic because of magnetorquers Sun because no eclipse during orbit
Actuator	3 magnetorquers	2 reaction wheels	Underactuation of magnetorquers

Table 1: Mandatory requirements for the project

3. Framework Analysis

3.1. Satellite characterization

The satellite design was inspired by ESAIL, a microsatellite developed by exactEarth in cooperation with ESA. ESAIL was primarily developed for ship targeting.^[1] Two configurations of the satellite were implemented: the undeployed configuration for the detumbling phase and the extended configuration for the slew and tracking phase. The deployed configuration is modeled as a cubic central body of side 70 cm and four solar panels, modeled as rectangular bodies of dimensions $70 \times 70 \times 1 \text{ cm}^3$. Solar panels are set along y_B axis of body frame B with the normal of surface parallel to z_B axis, as shown in Figure 1.

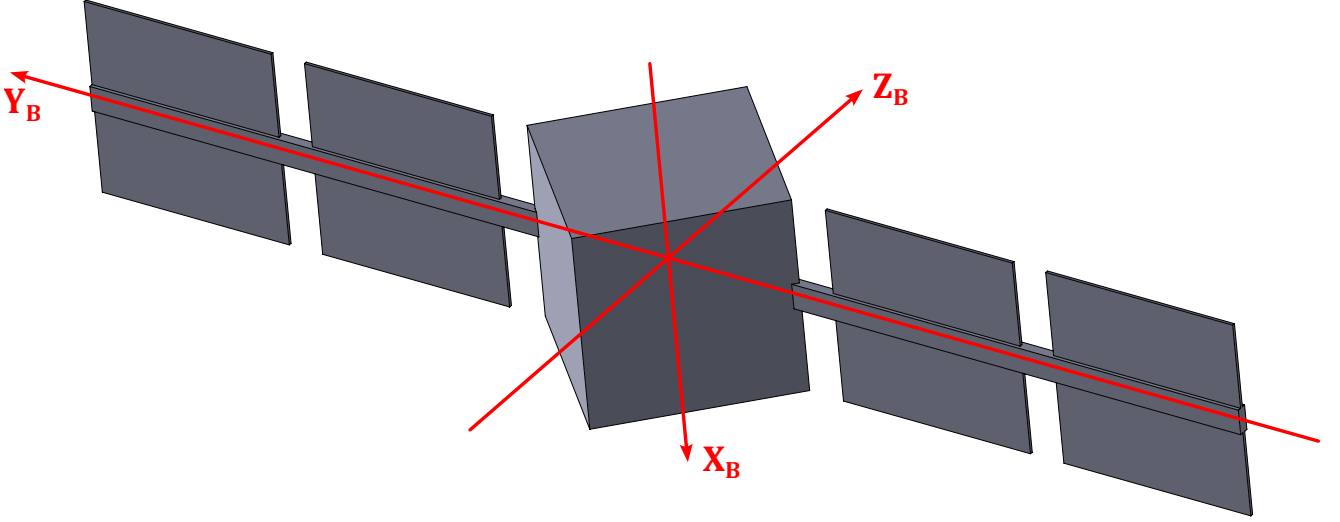


Figure 1: CAD model of the satellite

The mass is assumed to be 100 kg with isotropic distribution for simplicity. The inertia matrix results to be:

$$I = \begin{bmatrix} 22.9724 & 0 & 0 \\ 0 & 7.7770 & 0 \\ 0 & 0 & 23.1895 \end{bmatrix} \text{ kg/m}^2 \quad (1)$$

The undeployed configuration is an isotropic cube of side 70 cm with the same mass. The inertia matrix of this undeployed configuration is then:

$$I = \begin{bmatrix} 8.1667 & 0 & 0 \\ 0 & 8.1667 & 0 \\ 0 & 0 & 8.1667 \end{bmatrix} \text{ kg/m}^2 \quad (2)$$

3.2. Orbit characterization

The orbit adopted for the simulation is a nearly polar, LEO, Sun-synchronous orbit (SSO). Polar orbits allows to scan the whole globe during several orbits thanks to Earth's rotation. SSO are orbits that maintain the same angle between their orbital plane and the direction that connects the Earth with the Sun.^[2] This allows the spacecraft to monitor the Earth surface with the same conditions of light (or eventually darkness if the plane is oriented in a certain way). Furthermore, a SSO can be selected to ensure constant visibility on the Sun.^[3]

The orbital data are based on the ephemeris of an ESAIL mission taken at 12:00 UT on December 16th, 2023. The orbit was then propagated using the simple two-body problem without any perturbations.

This is an approximation as several disturbances act on the satellite (as discussed in section 6). Using the ephemeris as the initial condition has the advantage of allowing the simulation of spacecraft motion in two or three periods of the orbit to be considered as Sun-synchronous. This is because the time of simulation is a snapshot compared to the time of action of the J2 effect responsible for the Sun-synchronous orbit, which is one year. Clearly, a more detailed simulation should consider the variation of the orbital parameters due to J2 and all the other perturbations.

The orbital parameters chosen as described above are the following:

a [km]	e [-]	i [deg]	ω [deg]	Ω [deg]
6851	0.0018	97.40	101.58	0

Table 2: Orbital parameters

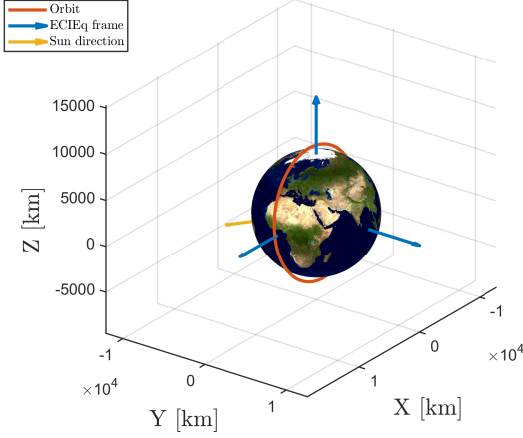


Figure 2: Orbit representation

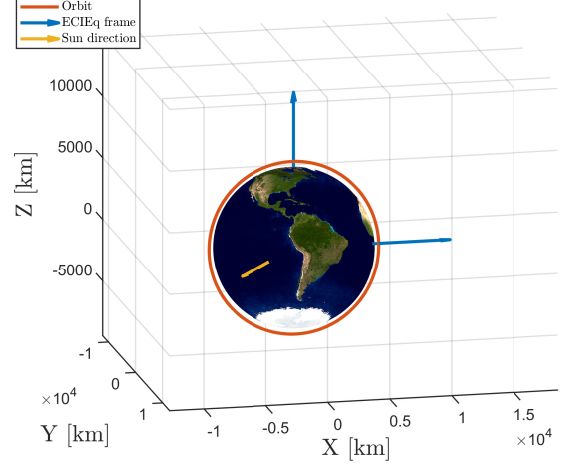


Figure 3: View from Sun direction

In Figure 2 and Figure 3 the Sun direction is plotted. This direction was computed by taking the ephemeris of the Earth with respect to the Sun at 12:00 UT December 16th in the Earth centered Equatorial frame. Since the orbital periods considered are relatively small compared to the Sun's motion, its position was maintained constant during the simulation. It's easy to see that the orbit never goes into eclipse condition.

On Simulink, the model implemented to retrieve the orbital position is based on the integration of the true anomaly:

$$\dot{\theta} = \frac{n(1 + e \cos \theta)^2}{(1 - e^2)^{3/2}} \quad (3)$$

Then, the radial distance is computed as:

$$r = \frac{a(1 - e^2)}{1 + e \cos \theta} \quad (4)$$

At this point it is easy to retrieve the position \mathbf{r}_P of the satellite in the perifocal frame \mathcal{P} :

$$\mathbf{r}_P = r \begin{bmatrix} \cos \theta \\ \sin \theta \\ 0 \end{bmatrix} \quad (5)$$

The position in the inertial frame \mathcal{N} is calculated using the transpose of the rotation matrix $A_{PN} = \mathbf{R}_3(\omega) \mathbf{R}_1(i) \mathbf{R}_3(\Omega)$:

$$\mathbf{r}_N = A_{PN}^T \mathbf{r}_P \quad (6)$$

4. Dynamics

The equations of dynamics adopted for a rotating rigid body motion are the Euler equations. The set of equations are referred to the principal inertia axis frame of the satellite. This frame coincides with the body frame \mathcal{B} previously defined (subsection 3.1). It is described by three unit vectors $\{\mathbf{x}_B, \mathbf{y}_B, \mathbf{z}_B\}$ that are in the direction of principal inertia axis of the satellite.

$$\mathbf{I} \dot{\boldsymbol{\omega}} + \boldsymbol{\omega} \times \mathbf{I} \boldsymbol{\omega} = \mathbf{M}_d + \mathbf{M}_c \quad (7)$$

In Equation 7 the external torque is split into two contributions. \mathbf{M}_d describes the disturbance torques acting on the spacecraft due to environment, it is treated in more detail in section 6. \mathbf{M}_c is referred to the control torque that the actuators generate in order perform the tasks required by the control logic (see section 10).

With particular reference to the Simulink model, the two different configurations of the satellite are considered: undeployed configuration for detumbling phase and extended configuration for slew and tracking.

Since the inertia matrix of the system must switch from Equation 2 to Equation 1, a logic switch has been implemented during the simulation, with the use of a flag based on the activation of the detumbling control. This instantaneous switch is not completely realistic since the extraction of the panels would require some finite time and could influence the real dynamic of the satellite. Anyhow, for the microsat considered, the retracted configuration allows a faster detumbling and also reduces the inertia loads and stresses on the solar panels and the structure.

5. Kinematics

As specified in section 2, the attitude parameters of the satellite are expressed through the use of Euler angles. The kinematics calculated according to this parameterization follows these steps:

- given the angular velocity ω from dynamics for each time and the initial condition on Euler angles s_0 , compute the time derivatives of the angles \dot{s} ;
- integrate the derivatives to obtain the set of Euler angles s for each time;
- from the calculated angles, compute the attitude matrix A_{BN} .

When dealing with this type of parameterization, a major issue arises due to the singularity conditions on the second angle θ for any chosen set of three Euler angles. This can cause the derivatives of the other two angles to tend towards infinity. The problem is a result of the fact that, under these specific conditions, the set of Euler angles is not uniquely defined, as the first and third rotations are performed on the same physical direction.

To avoid these singularities, it becomes necessary to have two systems working on two different sets of Euler angles:

- one set of angles defined by three different indexes, which has the singularity condition on $\theta = (2n + 1)\pi/2$;
- one set of angles where the first and the last indexes coincide, which has the singularity condition on $\theta = n\pi$;

with $n \in \mathbb{N}$. To merge these two systems and avoid singularities, there are two main options:

- run both systems all the time, get the attitude kinematics only from one system until it reaches its singularity condition on θ , then switch to the other system, which will be further from its singularity;
- run just one system at a time; when the system reaches its singularity condition, convert from the current set of angles to the other set through the attitude matrix, impose the calculated angles as initial condition on the other system, then start the integration from where it was interrupted, deactivating the system that reached the singularity.

Although the first option is simpler, the second option offers significant computational savings for the simulation. It is important to note that the kinematics model is only executed in the simulation to calculate the satellite's motion over time and is not executed on the satellite processor. Despite the added complexity of the system switch, the second option was chosen to accelerate the execution of the Simulink model.

In the model discussed in this report, the 312 and 313 sets of Euler angles were chosen. The equations for the integration and the conversion to attitude matrix are reported below:

$$\begin{cases} \dot{\phi}_{312} = \frac{\omega_z \cos \psi - \omega_x \sin \psi}{\cos \theta} \\ \dot{\theta}_{312} = \omega_x \cos \psi + \omega_z \sin \psi \\ \dot{\psi}_{312} = \omega_y - (\omega_z \cos \psi - \omega_x \sin \psi) \tan \theta \end{cases} \quad A_{312} = \begin{bmatrix} \cos \psi \cos \phi - \sin \psi \sin \phi \sin \theta & \cos \psi \sin \phi + \sin \psi \cos \phi \sin \theta & -\sin \psi \cos \theta \\ -\sin \phi \cos \theta & \cos \phi \cos \theta & \sin \theta \\ \sin \psi \cos \phi + \cos \psi \sin \phi \sin \theta & \sin \psi \sin \phi - \cos \psi \cos \phi \sin \theta & \cos \theta \cos \psi \end{bmatrix} \quad (8)$$

$$\begin{cases} \dot{\phi}_{313} = \frac{\omega_x \sin \psi + \omega_y \cos \psi}{\sin \theta} \\ \dot{\theta}_{313} = \omega_x \cos \psi - \omega_y \sin \psi \\ \dot{\psi}_{313} = \omega_z - (\omega_x \sin \psi + \omega_y \cos \psi) \cot \theta \end{cases} \quad A_{313} = \begin{bmatrix} \cos \psi \cos \phi - \sin \psi \sin \phi \cos \theta & \cos \psi \sin \phi + \sin \psi \cos \phi \cos \theta & \sin \psi \sin \theta \\ -\sin \psi \cos \phi - \cos \psi \sin \phi \cos \theta & -\sin \psi \sin \phi + \cos \psi \cos \phi \cos \theta & \cos \psi \sin \theta \\ \sin \phi \sin \theta & -\cos \phi \sin \theta & \cos \theta \end{bmatrix}$$

In order to translate one set of Euler angles to the other set is sufficient to remember that A_{312} must be equal to A_{313} , since attitude matrices are both related to the same physical object. Inverting the formulas:

$$\begin{cases} \phi_{312} = \text{atan2}(-A^{2,1}, A^{2,2}) \\ \theta_{312} = \arcsin(A^{2,3}) \\ \psi_{312} = \text{atan2}(-A^{1,3}, A^{3,3}) \end{cases} \quad \begin{cases} \phi_{313} = \text{atan2}(A^{3,1}, -A^{3,2}) \\ \theta_{313} = \arccos(A^{3,3}) \\ \psi_{313} = \text{atan2}(A^{1,3}, A^{2,3}) \end{cases} \quad (9)$$

The system switcher has been designed in Simulink using basic boolean operators. These operators are combined to generate a 'flag' signal that selects the appropriate system, taking into account the singularity conditions of both. In more detail, the switcher logic takes as input three boolean signals:

- $|\cos \theta_{312}| < \text{tol}$, where tol is a chosen tolerance value to keep the 312 system distant from the singularity;
- $|\sin \theta_{313}| < \text{tol}$, where tol is a chosen tolerance value to keep the 313 system distant from the singularity;
- the **flag** of the system at the previous step time.

A truth table can be created using the given signals and expected output. The truth table can then be simplified using basic logic operators such as AND, OR, and NOT through boolean algebra. Finally, the logic can be implemented in the simulation to handle the activation of the two systems.

6. Disturbances analysis

In order to make a realistic simulation of the rotating motion of the spacecraft, the disturbances caused by the environment must be taken into account. The following paragraphs provide a brief introduction to the main disturbances acting on the system. The simulation results for the chosen satellite and orbit will then be presented to aid in the selection of the two most significant disturbances. Since the other disturbances are typically much smaller than the dominant ones (often by some orders of magnitude), they will be disregarded in the final simulation.

6.1. Magnetic Disturbance

The influence of the Earth's magnetic field on the satellite is relevant due to the proximity of the orbit taken in exam. Besides the crucial role that it plays in the actuation, the magnetic field could also cause relevant disturbances on the satellite's dynamics. The magnetic torque, whether generated by the magnetorquers or by parasitic currents present in the satellite, follows the general law:

$$\mathbf{M} = \mathbf{D} \times \mathbf{B} \quad (10)$$

where \mathbf{D} is the magnetic dipole generated by a coil or by parasitic currents, \mathbf{B} is the magnetic field vector of Earth. A mathematical model of the magnetic field is necessary to evaluate \mathbf{B} given the satellite position along the orbit. The model chosen for the purpose is the 13th edition of the International Geomagnetic Reference Field (IGRF). According to this model, the magnetic field \mathbf{B} is evaluated as the gradient of a magnetic scalar potential V , which is modelled as a spherical harmonic expansion of order N :

$$\mathbf{B}(r, \theta, \phi, t) = -\nabla V(r, \theta, \phi, t) \quad V(r, \theta, \phi, t) = a \sum_{n=1}^N \sum_{m=0}^n \left(\frac{a}{r}\right)^{n+1} (g^{n,m}(t) \cos m\phi + h^{n,m}(t) \sin m\phi) P^{n,m}(\cos \theta) \quad (11)$$

where r, θ, ϕ are the spherical coordinates of the satellite in a Earth-Centered Earth-Fixed (ECEF) frame, a is the Earth's equatorial radius (6371.2 km), $P^{n,m}(\cos \theta)$ are the Gauss normalized associated Legendre functions, $g^{n,m}(t)$ and $h^{n,m}(t)$ are the Schmidt semi-normalized spherical harmonic coefficients. These coefficients are computed from experimental data and depend on time, as the Earth magnetic field is not constant but changes significantly every year. In this simulation, the coefficients refer to year 2020 of IGRF-13 and the expansion is computed up to order 13. Note that the model must be in the ECEF frame because the magnetic field rotates with the Earth. To adapt the model to an Earth-Centered Inertial (ECI) frame, a rotation matrix is required for the input and its transpose for the output. The matrix takes account of the angular velocity of Earth on time. Lastly, the magnetic field \mathbf{B} can be expressed in the body frame through the attitude matrix.

Once that \mathbf{B} is defined for every satellite position, the \mathbf{D} vector is chosen as an arbitrary constant (based on typical microsat values) and the torque is easily computed along the orbit thanks to Equation 10.

6.2. SRP Disturbance

The Solar Radiation Pressure (SRP) torque is the disturbance generated by electromagnetic waves that impact on the spacecraft panels generating force. These forces acting on some of the panels can rise a net torque around the center of mass of the spacecraft. For this analysis, only the Sun radiation is considered, while a more rigorous study should also consider the infrared radiation emitted by the Earth and the radiation of the Sun reflected by the Earth. Moreover, no eclipse condition is analyzed during the simulation, which is a reasonable assumption given the SSO chosen in subsection 3.2.

The formula to calculate the force acting on each discrete panel i is the following:

$$\mathbf{F}_i = -PA_i (\hat{\mathbf{S}}_B \cdot \hat{\mathbf{N}}_{B,i}) \left[(1 - \rho_s) \hat{\mathbf{S}}_B + \left(2\rho_s (\hat{\mathbf{S}}_B \cdot \hat{\mathbf{N}}_{B,i}) + \frac{2}{3}\rho_d \right) \hat{\mathbf{N}}_{B,i} \right] \quad (12)$$

In order to simulate this kind of disturbance, the coefficients of absorption ρ_a , specular reflection ρ_s and diffusion ρ_d must be decided. Since these three parameters are related through an energetic balance as $\rho_a + \rho_d + \rho_s = 1$, only two of them are independent while the third follows. These values clearly depend on the material of the main body and the solar panels of the spacecraft. In order to determine the force on each surface, the geometry of the panels of the satellite must be given (subsection 3.1), in particular the surface of each panel S_i and direction of the normal of the panel $\hat{\mathbf{N}}_{B,i}$ expressed in \mathcal{B} frame. The direction of Sun $\hat{\mathbf{S}}_B$ is modeled in ECI frame considering the obliquity $\epsilon = 23.44$ deg of Earth's rotation axis with respect to the ecliptic plane, then it is rotated in \mathcal{B} frame through the attitude matrix.

Lastly, to be able to compute the torque it must be known where the resulting force acts on each panel (i.e. the centre of SRP force of the panel). It is assumed as a first approximation that the forces act on the geometric center of the corresponding plate. In order to correctly calculate the total torque, a shadow check must be performed. This has been implemented in Simulink by checking the sign of the dot product between the normal versor of the plate $\hat{\mathbf{N}}_{B,i}$ and the Sun direction $\hat{\mathbf{S}}_B$.

6.3. Drag Disturbance

Over extended periods, the spacecraft's engagement with the higher strates of Earth's atmosphere results in the generation of a torque around its center of mass. At altitudes less than 400 kilometers, the aerodynamic torque is usually the predominant factor, though its significance diminishes considerably beyond 700 kilometers of altitude. For the simulation, the geometry of the panels is defined in [subsection 3.1](#). The coefficient of drag C_D is set to 2.2, the relative velocity considers both the rotation of Earth around its axis and the rotation motion of the spacecraft. As for the SRP case ([subsection 6.2](#)), a sort of shadow check has been implemented based on the dot product between the relative velocity and the normal of the surface. This check is necessary since only the exposed-to-air surfaces give the contribution to generate the drag force. As for SRP torque, the position of the center of action of the force \mathbf{r}_i should be evaluated for each panel. As a first approximation, the resulting force is placed in the geometric center of the panel.

$$\mathbf{M} = \begin{cases} \sum_{i=1}^n \mathbf{r}_i \times \mathbf{F}_i & \text{if } \hat{\mathbf{N}}_{B,i} \cdot \hat{\mathbf{v}}_{B,i}^{rel} \geq 0 \\ \mathbf{0} & \text{if } \hat{\mathbf{N}}_{B,i} \cdot \hat{\mathbf{v}}_{B,i}^{rel} < 0 \end{cases} \quad \text{with} \quad (13)$$

$$\mathbf{F}_i = -\frac{1}{2} \rho C_D \|\mathbf{v}_{B,i}^{rel}\|^2 (\hat{\mathbf{N}}_{B,i} \cdot \hat{\mathbf{v}}_{B,i}^{rel}) A_i \hat{\mathbf{v}}_{B,i}^{rel} \quad n = \text{number of faces}$$

The air density ρ is computed according to the US Standard Atmosphere of 1976. The model uses an exponential law to describe ρ as a function of altitude h :

$$\rho = \rho_0 \cdot \exp\left[-\frac{h-h_0}{H}\right] \quad (14)$$

Considering the orbit defined in [subsection 3.2](#), the range of altitude is between 450 and 500 km. From this information, the constants of the formula are the following^[4]:

$$\rho_0 = 1.585 \cdot 10^{-12} \text{ kg/m}^3 \quad h_0 = 450 \text{ km} \quad H = 60.828 \text{ km}$$

6.4. Gravity Gradient Disturbance

Since the gravity around the spacecraft is not uniform, a non-negligible gravity torque will arise from there. Studying the torque generated by an elementary force acting on the elementary mass dm the [Equation 15](#) is obtained:

$$d\mathbf{M} = -\mathbf{r} \times \frac{Gm_t dm}{\|\mathbf{R} + \mathbf{r}\|^3} (\mathbf{R} + \mathbf{r}) \quad (15)$$

where \mathbf{r} is the position vector of dm from the center of mass and \mathbf{R} is the position vector of the center of mass from the center of Earth. Approximating this equation and expressing the position vector of the centre of mass as the product of magnitude (R) with the direction cosines, it's possible to centre this torque in the principal inertia axes. Integrating this equation the final form is achieved.

$$\begin{aligned} M_x &= \frac{3Gm_t}{R^3} (I_z - I_y) c_2 c_3 \\ M_y &= \frac{3Gm_t}{R^3} (I_x - I_z) c_1 c_3 \\ M_z &= \frac{3Gm_t}{R^3} (I_y - I_x) c_1 c_2 \end{aligned} \quad (16)$$

c_1, c_2 and c_3 are the direction cosines of the radial direction in the principal axes. Therefore, if one of the principal axes is aligned with the radial direction, the torque will be zero because only one of the direction cosines would be non-zero. It's clear that this disturbance acts in a continuous manner throughout the orbit motion and the torque produced depends mainly on the attitude matrix.

Instead, the stability configuration depends only on the distribution of mass of the spacecraft with respect to the target orientation. For this case of study the satellite is nadir pointing, so \mathbf{x}_b has to be aligned with the nadir while \mathbf{z}_b has to be normal with respect to the orbital plane. Using the numerical values of the spacecraft and the orientation requirements just mentioned, this particular configuration results to be unstable to GG disturbance.

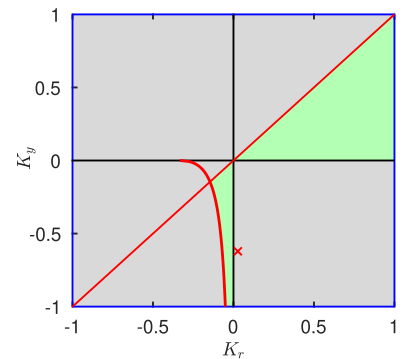


Figure 4: GG stability of satellite

6.5. Simulation of all disturbances

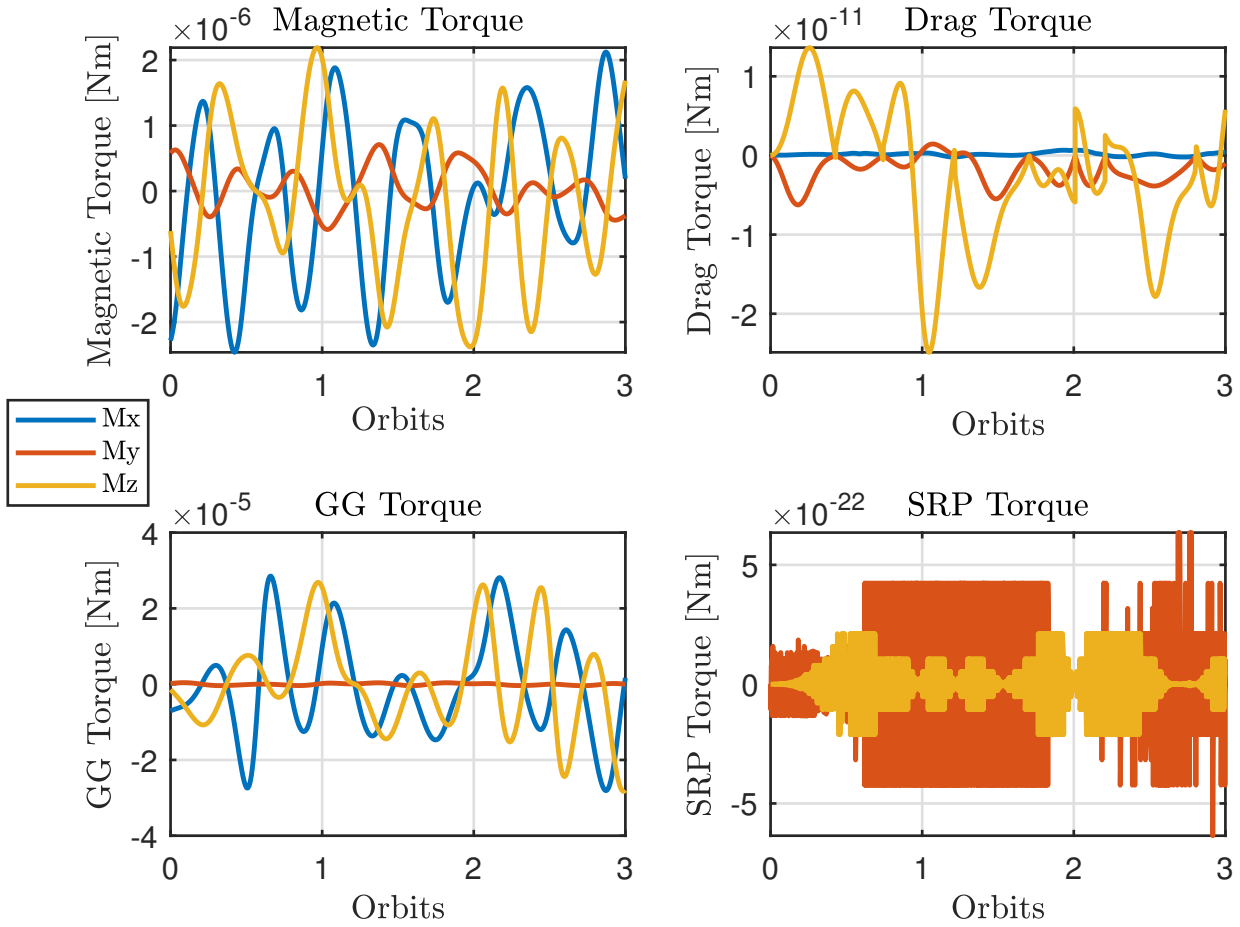


Figure 5: Simulation of all disturbances

The control-free motion was simulated with all the disturbances for three full periods. The initial conditions were set to null initial angular velocity and null Euler angles in the 312 set, in order to be in operational behaviour.

From the graphs of Figure 5 it is clear that SRP disturbance is negligible, as the graph shows only numerical zeros. In particular, this is due to the geometrical symmetry of the spacecraft. A small set off of the centre of mass would have produced a net torque. It is clear that, in this specific case, the two most relevant disturbances are due to magnetic field interaction and gravity gradient torque since the atmospheric drag torque is some orders of magnitude smaller. Note that in the gravity gradient torque the y-axis component is almost null compared to the other components along x and z. This is due to the fact that the y-axis component of the torque depends on the difference between the inertia moments along x and along z, and in this case those two moments of inertia are very similar (see subsection 3.1).

7. Sensors

Sensors are fundamental tools that allows the S/C to know its orientation and angular velocity. Their presence onboard is fundamental for achieving a controlled motion of the satellite. In this section, the three chosen sensors will be presented. It will be also clarified the motivation that lead the team to choose two additional sensors over the horizon sensor assigned.

7.1. Horizon Sensor

Horizon sensors are devices that can detect the centre of the planet, in this case the Earth, and reconstruct the direction of that point with respect to the satellite. They usually work by analyzing the IR spectrum of the image through a thermopile to reduce the visible light spectrum interference caused by transition of day and night on Earth. Due to the nadir pointing requirement, a static Earth sensor was chosen for this specific application, in particular the *Meisei Earth Horizon*, that has the following specifics^[5]:

<i>F.O.V.</i> [deg]	<i>Accuracy</i> [deg]	<i>Frequency</i> [Hz]
33	1	30

Table 3: Principal parameters of Horizon Sensor

Due to operational requirements, the static sensor has to point the Earth, in particular the optical axis must have the same direction of the nadir (direction that links centre of Earth and CoM of the S/C). To fulfill the request, a good option could be to position the sensor on the face that also contains the payload, that is the face of the spacecraft that has normal along the x_b direction.

The model implemented to simulate the behaviour of the sensor in the Simulink environment takes the real position of the S/C with respect to centre of Earth expressed in inertial space, changes its direction and expresses it in the \mathcal{B} frame through the real attitude matrix A_{BN} . This unit vector is the input of the sensor block, where it is sampled through a zero-order hold of frequency specified by Table 3 to simulate the digital nature of the sensor. Then some errors of measurements must be added. It was decided to model two typical effects of real sensor: the mounting error that causes a misalignment and also an accuracy error modeled with a band-limited white noise on all the components of the direction vector. Chronologically, firstly the misalignment is calculated, then the noise is introduced.

- The misalignment error was computed on Simulink by introducing a small deviation with respect to the nominal condition. This can be done by adding a small-scaled vector in the perpendicular direction of the unit vector that has to be measured. The amplitude of this vector has to be small with respect to the unit direction considered by the measure. Since the vector of the measured direction is initially unitary, the length of the bias vector introduced can be considered as $\tan \theta_{small} \approx \theta_{small}$, where θ_{small} represents the angle between real measure and misaligned measure.
- In the Simulink environment, the white noise has to be defined through the noise power. This was computed as $N_p = \sigma^2 T_s$, where σ^2 represents the variance as the standard deviation squared, while T_s is the sampling time of the sensor. It was decided to consider as standard deviation the accuracy from Table 3.

7.2. Magnetometer

Since from subsection 6.5 the magnetic field resulted to be one of the main disturbances, the magnetometer is a must-have on the satellite. This kind of sensor are in general less accurate than optical sensors as the Sun sensor or the star sensor, but since the magnetic field of a LEO is effectively strong enough, the sensor can provide always a sufficiently good measure. Furthermore, having a magnetorquer assigned as mandatory, the coupling of this actuator with a magnetometer can be exploited during the de-tumbling manoeuvre through a direct dipole command. This technique is the so-called *B-dot control*, extensively discussed in subsection 10.1.

The fluxgate magnetometer typology was used where, for each body axis, two ferromagnetic cores are placed parallel to that specific axis. The primary coil saturates the two bars alternatively in opposite directions, so that the secondary output theoretically can read a null induced voltage output produced by the time-varying flux. When an external field is present, the symmetry of the alternate saturation is broken so that a shift on the magnetic flux of the secondary coil is produced. This net flux can be read by the time-history of a voltmeter on the secondary coil, since the spacing of the measured output voltage depends on the external magnetic field value.

Since magnetometer are usually characterized by low accuracy values, a deep search has been conducted to find a high-accuracy and low-noise typology. A suitable sensor is the MM200 furnished by AAC ClydeSpace. The following performance parameters characterize this sensor:

<i>NSD</i> [nT/ $\sqrt{\text{Hz}}$]	<i>Frequency</i> [Hz]
1.18	30

Table 4: Principal parameters of Magnetometer

For the Simulink model, the same approach as the horizon sensor in subsection 7.1 was used. In particular, the magnetic field vector coming from the block discussed in subsection 6.1 was transformed into \mathcal{B} reference frame through the attitude matrix. This is the input vector that has to be sampled with the frequency specified by Table 4. For this specific sensor, a range of frequencies could be chosen: it was chosen to maintain the same frequency as the horizon sensor from Table 3, as it respects the constraint given by the magnetometer.

Then the measurement errors have to be added: a first misalignment error is modeled in the same way as the horizon sensor in subsection 7.1. The accuracy error, induced by the noise, was modeled through a band-limited white noise added on each component. The value of N_p is the square of NSD presented in Table 4.

7.3. Sun Sensor

Sun sensors are devices that detect the position of the Sun by measuring the incidence angle of its radiation on a sensor surface. This surface is typically made of materials that can generate a current proportional to the intensity of the incident light. From the measure of the current I generated by the sensor surface of area S , knowing the intensity of the radiation W and the coefficient α of the sensor, the angle of the incident light θ is internally computed as:

$$I = \alpha S W \cos \theta \implies \theta = \arccos\left(\frac{I}{\alpha S W}\right) \quad (17)$$

The unit vector pointing towards the Sun can be easily computed by the sensor using the knowledge of two angles obtained by placing two surfaces on different directions of the same plane.

As discussed in [section 3](#), the satellite mission consists in pointing the Earth on a Sun-synchronous orbit without any eclipse periods. Therefore, accuracy should be prioritised over having the best Field of View (FOV) when selecting the sensor. For this reason, the choice falls upon a small and light Fine Sun sensor with good performances such as the AAC Clyde Space SS200^[6]:

<i>F.O.V.</i> [deg]	<i>Accuracy</i> [deg]	<i>Frequency</i> [Hz]
90	0.3	30

Table 5: Principal parameters of Sun Sensor

This sensor has to be placed in the same direction as the solar panels (i.e. in the \mathbf{z}_b direction) so the Sun is constantly visible (since the orbit is Sun-synchronous). To avoid unnecessary complexity in the Simulink model, the sensor's field of view is not taken into consideration. This is because the sensor is not used during the detumbling manoeuvre, while in the tracking phase the Sun is always visible. To simulate the output of the real sensor, the model uses the Sun direction calculated by adding the initial Earth-Sun vector to the position vector of the satellite in the inertial frame, which is computed through Keplerian dynamics. The resulting vector is then normalized, reversed, and transformed into the body frame using the attitude matrix. From here, errors have been added in the same manner as described for the horizon sensor ([subsection 7.1](#)).

8. Attitude determination

The problem of estimating the attitude matrix from the available measurements is central to spacecraft control. To determine the attitude of the spacecraft, the sensor models introduced earlier were used. The method used to determine the attitude is the SVD method^[7], which has been developed within the framework of Wahba's problem. The latter consists in finding the orthogonal matrix which minimizes the weighted cost function:

$$J(\mathbf{A}_{BN}) = \frac{1}{2} \sum_{i=1}^N \alpha_i \|\mathbf{s}_i - \mathbf{A}_{BN} \mathbf{v}_i\|^2 \quad (18)$$

in which $\{\mathbf{s}_i\}$ is a set of the N measured unit vectors in body frame and $\{\mathbf{v}_i\}$ is the corresponding set of unit vectors in the inertial frame, computed using the on-board models. The set of weights $\{\alpha_i\}$ were chosen basing on the relative accuracy of each sensor. It was assumed that the weight vector α is normalized to 1, i.e. $\sum_{i=1}^N \alpha_i = 1$. This method needs at least two available measurements, so it works also in the case that the Earth is outside the FOV of the horizon sensor.

Since \mathbf{A}_{BN} is an orthogonal matrix while \mathbf{s}_i and \mathbf{v}_i are unit vectors, through some simple algebraic passages it is possible to rewrite the expression of J as:

$$J(\mathbf{A}_{BN}) = 1 - \sum_{i=1}^N \alpha_i (\mathbf{s}_i^T \mathbf{A}_{BN} \mathbf{v}_i) \quad (19)$$

The optimal solution minimizes J , therefore it maximizes \tilde{J} :

$$\tilde{J}(\mathbf{A}_{BN}) = \sum_{i=1}^N \alpha_i (\mathbf{s}_i^T \mathbf{A}_{BN} \mathbf{v}_i) = \text{Tr}(\mathbf{A}_{BN} \mathbf{B}^T) \quad (20)$$

where Tr is the trace operator and $\mathbf{B} = \sum_{i=1}^N \alpha_i \mathbf{s}_i \mathbf{v}_i^T$.

Since a direct solution is computationally expensive, a single value decomposition technique is used. The matrix \mathbf{B} can be decomposed as:

$$\mathbf{B} = \mathbf{U} \mathbf{S} \mathbf{V}^T = \mathbf{U} \text{diag}([\mathbf{s}_1 \ \mathbf{s}_2 \ \mathbf{s}_3]) \mathbf{V}^T \quad (21)$$

U and V are orthogonal matrices, representing the matrices of eigenvectors of BB^T and B^TB respectively, S is the diagonal matrix containing the square roots of the eigenvalues of B^TB . Also other two matrices can be defined:

$$U_+ = U \text{diag}([1 \ 1 \ \det(U)]) \quad \text{and} \quad V_+ = V \text{diag}([1 \ 1 \ \det(V)]) \quad (22)$$

Then:

$$B = U_+ S' V_+^T = B = U_+ \text{diag}([s_1 \ s_2 \ s'_3]) V_+^T \quad (23)$$

where:

$$s'_3 = s_3 \det(U) \det(V) \quad (24)$$

Now it can be defined the matrix W and its representation in terms of Euler axis/angle:

$$W = U_+^T A V_+ = \cos\theta I_3 - \sin\theta [e \times] + (1 - \cos\theta) e e^T \quad (25)$$

$$\text{Tr}(AB^T) = \text{Tr}(WS') = e^T S' e + \cos\theta (\text{Tr}(S') - e^T S' e) \quad (26)$$

The trace is maximized for $\theta = 0$, which gives $W = I_3$ and thus the optimal attitude matrix is:

$$A = U_+ V_+^T = U \text{diag}([1 \ 1 \ \det(U)\det(V)]) V^T \quad (27)$$

Since sensor's measurements are affected by noise, a discrete low-pass Butterworth filter was added just after the calculation of the attitude matrix. The cut-off frequency was set to 0.5 rad/s for a 2nd order filter.

As previously mentioned, the weights required to construct the B matrix are determined by the relative accuracy of each sensor. As no data regarding the magnetometer's accuracy in degrees was provided, the following procedure was used to reconstruct its relative accuracy and assign a weight to each sensor. A period of three orbits was simulated, assuming to be already in the tracking phase, in order to be sure to be in the FOV of the Earth horizon sensor. During the simulation it was computed the angle ϕ between the ideal unit vector and the measured one. For instance, when discussing the magnetometer, ϕ represents the angle between the unit vector parallel to the magnetic field and the unit vector measured by the magnetometer. For each sensor ϕ is a random number, it was then computed the expected value and the standard deviation using the formulas reported below:

$$E[\phi] = \frac{1}{3T} \int_0^{3T} \phi dt \quad \sigma_\phi^2 = \frac{1}{3T} \int_0^{3T} (\phi - E[\phi])^2 dt \quad \sigma_\phi = \sqrt{\sigma_\phi^2} \quad (28)$$

where T is the period of the orbit. The integrals were evaluated numerically. The results obtained are reported in Table 6:

Sensor	$E[\phi]$ [deg]	σ_ϕ [deg]
Magnetometer	0.0089	0.0078
Sun Sensor	0.3124	0.2720
Earth Sensor	1.1301	0.8544

Table 6: Expected value and standard deviation calculated

Based on Table 6, it was chosen the weights α_1 used in the attitude determination with three sensors and the weights α_2 used in the attitude determination with two sensors. The values are reported in Table 7:

Sensor	α_1 [-]	α_2 [-]
Magnetometer	0.80	0.80
Sun Sensor	0.15	0.20
Earth Sensor	0.05	—

Table 7: Weights α_1 and α_2

9. Actuators

9.1. Magnetorquers

Magnetorquers are actuators capable of inducing a torque on the spacecraft through the generation of a magnetic dipole, according to Equation 10. This dipole can be generated by an electrical current flowing into a coil, as stated in the Ampere-Maxwell equation from electromagnetism. To be capable of generating a \mathbf{D} vector in any direction of 3D space, three coils have to be placed on three perpendicular axis in order to generate three independent components of the magnetic dipole.

Nowadays, magnetorquers are probably the most used attitude control actuators. This is primarily due to their extreme versatility and inexpensiveness for little satellites orbiting sufficiently near to Earth. All this combined with their virtually unlimited lifetime (because they only need current which can come from solar energy) gives the magnetorquer a wide range of applicability. Moreover, they allow a smooth modulation of the control torque and they assure significant savings in terms of weight and complexity since no moving parts are present.

This comes clearly with some downsides. The most limiting factor for this type of actuator is the low torque generated, typically in the range of $10^{-3} \div 10^{-6}$ Nm, that could make the control action really slow, especially for more big and heavy satellites. Another limiting factor is of course the fact that they rely completely on the external magnetic field, which could vary a lot during the orbit and there could be zones in which the effectiveness is greatly reduced due to a weak \mathbf{B} vector. Furthermore, the satellite could be a source of disturbance due to some parasitic currents flowing in other electronic devices. The same could be said for the magnetic coils themselves, which can be source of disturbance for the magnetic sensors.

In addition of all this, the torque generated by these actuators cannot have three independent components, since the torque can be generated only in a plane perpendicular to \mathbf{B} vector of the magnetic field. This can be demonstrated from Equation 10, which is reported and expanded below:

$$\mathbf{M} = \mathbf{D} \times \mathbf{B} = [-\mathbf{B} \times] \mathbf{D} \implies \begin{bmatrix} M_x \\ M_y \\ M_z \end{bmatrix} = \begin{bmatrix} 0 & B_z & -B_y \\ -B_z & 0 & B_x \\ B_y & -B_x & 0 \end{bmatrix} \begin{bmatrix} D_x \\ D_y \\ D_z \end{bmatrix} \quad (29)$$

$$\mathbf{D} = [-\mathbf{B} \times]^{-1} \mathbf{M} \quad (30)$$

Since $[-\mathbf{B} \times]$ is a singular matrix, it cannot be inverted as shown in Equation 30, so the complete controllability of the system through magnetic actuators is not assured.

The magnetorquer that was selected for this project is the *MTQ800* from *ACC Clyde Space*, which details are reported below^[8]:

$D_{max} [Am^2]$	$frequency [Hz]$
15	30

Table 8: Principal parameters of Magnetorquer

The Simulink model takes as input the ideal dipole requested by the controller, elaborates it through a rate limiter and a saturation limiter, then it introduces some random white noise. This model, which has been used also for the other actuators, is designed to replicate the accuracy, the dynamics and the limits of the actuators in the real world. Otherwise, the control would be ideal and it could generate some torques that would be impossible to obtain with physical actuators.

9.2. Reaction Wheels

Reaction wheels are one of the primary attitude control actuators for controlling the spacecraft, as they are reliable and can give precise pointing. Their working principle is based on the internal angular momentum exchange between the satellite and the reaction wheel itself. At every time instant, the angular momentum of the overall system composed by the reaction wheel and the rest of the satellite can be expressed as:

$$\mathbf{h} = \mathbf{I}\boldsymbol{\omega} + \mathbf{h}_r \quad (31)$$

where \mathbf{h}_r is the angular momentum of the reaction wheel with respect to the rest of the spacecraft along its spin axis. If no external torque is applied, due to the conservation of angular momentum, it can be written:

$$\mathbf{I}\dot{\boldsymbol{\omega}} = -\dot{\mathbf{h}}_r \quad (32)$$

Usually $\dot{\mathbf{h}}_r$ is due to the torque applied to the reaction wheel by an electric motor, that has its proper operational curve. The latter can be modeled as constant until a certain angular velocity ω_{max} is reached by the reaction wheel.

When the saturation speed ω_{max} is achieved, the reaction wheel cannot provide any additional torque, either positive or negative. If the torque required is more or less periodic, it is possible to choose the actuator in order to have it always in the functioning regime. If, in addition to the periodical component, there is a secular contribution, then it is inevitable to reach the saturation speed. To avoid this, it is necessary a desaturation maneuver, executed with the help of the magnetorquers.

The model chosen for the reaction wheels is the *OCE-RW40*, which is characterized by the following specifications^[9]:

ω_{max} [RPM]	\dot{h}_{max} [Nm]	σ_{ω} [RPM]	frequency [Hz]
6000	0.1	2	30

Table 9: Principal parameters of Reaction Wheel

The Simulink model of the reaction wheel takes as input the ideal torque. The $\dot{\omega}_r$ is computed dividing by the inertia of the wheel around its spin axis. ω_r is computed integrating $\dot{\omega}_r$. $-\dot{h}_r$, which comes from the control block, is multiplied by the result of the boolean operation $\omega_r \leq \omega_{max}$. At this point, the signal passes through a rate limiter and a saturator. Lastly, a band limited white noise is added to the generated torque.

10. Control logic

The control logic of the satellite is implemented on the computer that handle all the on-board calculations. In particular, all the data from the in-FOV sensors has to be gathered. Then, based on the mission phase, the necessary control has to be calculated and the commands have to be sent to the system of actuators. The necessary control calculation is discussed in this section. Clearly, every phase of the mission is different, this is due to the mission requirements (i.e. detumble or pointing) or to the physical equations that describe the problem (linear or non-linear). Moreover, when a phase of the mission has to be analyzed and a control applied for it, all the possibilities and limitations coming from sensors and actuators have to be evaluated. As a consequence, the design of a control logic is strictly related to the implementation of the actuators in the system, since even though a perfect control u can be designed by placing the fastest poles (in the linear case), the actuators' system would be highly and would not be able to perform the requested torque. As a consequence, it is important to bear in mind when designing the control logic the kind of actuators that will be used.

In the case under analysis, the magnetorquers have some useful and powerful properties, as seen in subsection 9.1. In particular when they are coupled with a magnetometer, the theory tells that the de-tumbling phase can be easily implemented^[10]. On the other side, the control for a direction pointing (i.e. Nadir), in the case of magnetorquer is more difficult due to the unpleasant underactuation property of these magnetic systems. Indeed, considering the equation of the actuator for the magnetorquer and implementing that into the system equations would result into a instantaneously uncontrollable system as cited in^[11]. Nevertheless, by following the steps presented in^[11], a fully magnetic-actuated control could be reached but not without some effort and drawbacks. In order not to complicate the next discussion, it was chosen the take into consideration two reaction wheels as a secondary actuation system. In the next subsections the logic implemented in the Simulink environment will be presented, then more specific considerations on the actuators will be clarified.

10.1. De-tumbling phase: the B-dot control

The de-tumbling phase is performed immediately after the release of the spacecraft by the launcher. At this moment the angular velocity is random and depends on the launcher motion, and the attitude is also unknown. In order to make the satellite ready to enter in the operational regime so that it can start the pointing phase, the spacecraft must be de-tumbled. This means to create a control capable of decelerating the rotational velocities and fetch them to arbitrarily small values.

A frequently adopted solution on magnetic-actuated satellites is to implement the so-called *B-dot control*. This method exploits magnetic measurements to produce a direct magnetic dipole command to the magnetorquer that leads to arbitrarily small values of ω . Even though the magnetorquers have some problematics (as discussed in subsection 9.1), Avanzini et al.^[10] demonstrated that asymptotic stability can be reached using only a magnetorquer and a magnetometer through the following law:

$$D = -\frac{k_{\omega}}{\|B_B\|} \dot{B}_B \quad (33)$$

The idea of this kind of command is that the variation in magnetic field B in the B frame can be written as:

$$\dot{B}_B = \frac{d(A_{B,N} B_N)}{dt} = \dot{A}_{B,N} B_N + A_{B,N} \dot{B}_N \approx \dot{A}_{B,N} B_N = -[\omega \times] A_{B,N} B_N = -[\omega \times] B_B \quad (34)$$

The approximation symbol is due to the fact that when $\omega \gg 1$, the variation of the magnetic field vector in \mathcal{B} frame is mainly due to the rotation of the frame and less due to the changing of \mathbf{B}_N (that is caused by the evolution of the orbital position and other slow variations due to geomagnetic field). With the above equation it was demonstrated that ω and $\dot{\mathbf{B}}$ are strictly related, so making the control law proportional to $\dot{\mathbf{B}}$ would be similar to make it proportional to ω (like the 'standard' de-tumbling law). This mathematical considerations imply that for a detumbling law, it is sufficient to have a magnetometer and a magnetorquer without a direct measurement of the angular velocity obtainable by a gyroscope. Another positive consequence of having a proportional law that produces directly a magnetic dipole \mathbf{D} is that the command is directly made as an input of the actuator (without inverting any actuator law). It is important to underline that this kind of law would work at his best when angular velocity is high enough to make the assumption of Equation 34 true. In theory the actuated torque is:

$$\mathbf{M}_c = -\frac{k_\omega}{\|\mathbf{B}_B\|} \dot{\mathbf{B}}_B \times \mathbf{B}_B \quad (35)$$

It can be noticed that when $\omega \gg 1$, Equation 34 becomes more and more accurate, and so \mathbf{B}_B and $\dot{\mathbf{B}}_B$ are perpendicular, resulting in the maximum actuatable control torque.

Regarding the control law in Equation 33, note that the vector derived is not the derivative of the magnetic field vector, but it is the derivative of the unit vector of the magnetic field. It is important to notice that all the vectors in the above relationship are expressed in \mathcal{B} frame, since the magnetic field vector \mathbf{B} comes from the magnetometer.

In the context of the simulation environment on Simulink, the formulation chosen for the B-dot control comes from^[10]. Some precautions have to be taken when implementing the law, since the numerical derivative of a measured (hence noisy) signal has to be performed. This inconvenience can be overcome by using a low-pass filter^[7]. In Simulink, a discrete low-pass Butterworth filter of the 1st order has been used just after the discrete derivative block. Setting the cut-off frequency on 0.06 rad/s the signal is pretty clean and the results of simulation are coherent. Moreover, the gain value k_ω has to be defined. Avanzini et al.^[10] extensively discusses this parameter and propose a method for its characterization. The indicative formula is the following:

$$k_\omega = 2n(1 + \sin \xi) \min(I_x, I_y, I_z) \quad (36)$$

Where n represent the mean motion of the orbit, ξ the inclination of the orbit with respect to the magnetic equator. Notice that during the detumbling the inertia moments are all equal (Equation 2). The value obtained is:

$$k_\omega = 0.0363 \text{ kg} \cdot \text{m}^2 \text{s}^{-1}$$

10.2. Slew and Nadir pointing phases

10.2.1 Control law for the Slew and Tracking Manoeuvre

The goal for the control system in this phase is to track the \mathcal{LVCH} frame. In order to obtain the right alignment between the frames, both the attitude error and the angular velocity error should go to zero. Indeed, the tracking of \mathcal{LVCH} frame not only means to reduce the error angles but also to arrive at the aligned condition with the correct angular velocity in order to not overshoot the correct position. The attitude error matrix is \mathbf{A}_{BL} , which leads from the \mathcal{LVCH} to the body frame, and the goal is to make it close to the identity matrix. For this reason, the extra diagonal terms have to be close to zero, so the error vector was defined as:

$$\boldsymbol{\epsilon} = (\mathbf{A}_{BL}^T - \mathbf{A}_{BL})^V \quad (37)$$

The $[\cdot]^V$ operator is the inverse of $[\cdot \times]$, so it maps a skew-symmetric matrix back to its generating vector. The angular velocity error was defined as:

$$\boldsymbol{\omega}_{BL} = \boldsymbol{\omega} - \mathbf{A}_{BL} [0 \ 0 \ n]^T \quad (38)$$

For the case under analysis, in which the orbit is slightly elliptical, it would have been more precise to use the true anomaly rate $\dot{\theta}$ instead of the mean motion n in Equation 38. It was used n for simplicity, this doesn't affect the performance of the controller since the orbit is almost circular. $\boldsymbol{\omega}$ was obtained by taking the numerical derivative of the matrix \mathbf{A}_{BN} computed by the attitude determination algorithm, and then inverting the formula:

$$\dot{\mathbf{A}}_{BN} = -[\boldsymbol{\omega} \times] \mathbf{A}_{BN} \quad (39)$$

Since \mathbf{A}_{BN} is affected by noise, taking its derivative numerically amplifies it, leading to a bad estimation of the angular velocity. Therefore a discrete lowpass Butterworth filter was applied before the computation of $\boldsymbol{\omega}$. This was set as a 1st order filter with cut-off frequency at 1 rad/s. Once computed $\boldsymbol{\alpha}$ and $\boldsymbol{\omega}_{BL}$, a suitable control law is:

$$\mathbf{M}_c = -k_1 \boldsymbol{\epsilon} - k_2 \boldsymbol{\omega}_{BL} \quad (40)$$

This kind of control law is inspired by the linear full-state feedback control $\mathbf{u} = -\mathbf{k}\mathbf{x}$. In particular, it refers to the linearized Euler equations in which a set of three Euler angles α is introduced. This set of small angles represent the misalignment between \mathcal{B} and \mathcal{LVCH} frames. When this linearization is made, the state \mathbf{x} for the state-space formulation contains both α and $\dot{\alpha}$. If $\mathbf{u} = -\mathbf{k}\mathbf{x}$ is implemented with that state, the control law becomes a *Proportional-Derivative* control, in the form:

$$\mathbf{M}_c = -\mathbf{K}_p \alpha - \mathbf{K}_d \dot{\alpha} \quad (41)$$

Since the linear control theory allows to use different methodologies to calculate the gains matrices \mathbf{K}_p and \mathbf{K}_d , the linearized control law was firstly analyzed. In particular, the pole placement technique was used, on the following state-space representation of the system:

$$\begin{cases} \dot{\mathbf{x}} = \mathbf{A}\mathbf{x} + \mathbf{B}\mathbf{u} \\ \mathbf{y} = \mathbf{C}\mathbf{x} + \mathbf{D}\mathbf{u} \end{cases} \quad \mathbf{A} = \begin{bmatrix} 0 & (1-K_x)n & 0 & -n^2 K_x & 0 & 0 \\ (K_y-1)n & 0 & 0 & 0 & -n^2 K_y & 0 \\ 0 & 0 & 0 & 0 & 0 & 0 \\ 1 & 0 & 0 & 0 & 0 & 0 \\ 0 & 1 & 0 & 0 & 0 & 0 \\ 0 & 0 & 1 & 0 & 0 & 0 \end{bmatrix} \quad \mathbf{B} = \begin{bmatrix} \frac{1}{I_x} & 0 & 0 \\ 0 & \frac{1}{I_x} & 0 \\ 0 & 0 & \frac{1}{I_x} \\ 0 & 0 & 0 \\ 0 & 0 & 0 \\ 0 & 0 & 0 \end{bmatrix} \quad (42)$$

The first equation of the system represent the state space dynamics, which can be studied for the stability properties, while the second one represents the output coming from the sensors. The open-loop poles calculated for this system were:

$$\mathbf{p}_{open} = \begin{bmatrix} 0 \pm 0.0011i \\ 0 \pm 0.0002i \\ 0 \end{bmatrix} \quad (43)$$

The gain matrix $\mathbf{K} = [\mathbf{K}_d \ \mathbf{K}_p]$ was assessed through the MATLAB *place(A,B,p)* function, which requires the state-space matrices \mathbf{A} and \mathbf{B} , and also the desired closed-loop poles \mathbf{p} . At this point, this vector of six poles must be hypotized. Some precautions must be taken when the poles are decided:

- closed-loop poles shall not be too far from the corresponding open-loop poles, since there are constraints on the capabilities of the actuators;
- the real part of the closed-loop poles must be negative in order to guarantee asymptotic stability;
- the imaginary part of the poles should be decided in order to minimize the overshoot.

The chosen poles were:

$$\mathbf{p} = \begin{bmatrix} -0.02 \pm 0.1i \\ -0.01 \pm 0.06i \\ -0.05 \pm 0.1i \end{bmatrix} \quad (44)$$

The gain matrix can be used for the linear-control law. For simplicity, it wasn't used a matrix for the non-linear control but only a scalar. In particular, it was kept the order of magnitude coming from the gain matrix of the linear control just calculated. The values for the gains were then refined with trial and error. The response of the system was satisfactory with the following values:

$$k_1 = 0.001 \text{ kg} \cdot \text{m}^2 \text{s}^{-2} \quad k_2 = 0.6 \text{ kg} \cdot \text{m}^2 \text{s}^{-1}$$

10.2.2 Actuators' command logic for Slew and Nadir pointing

Once the control torque \mathbf{M}_c has been calculated, a logic was implemented to translate it into a command to be sent to the actuators. Magnetic actuators generate the torque with the formula

$$\mathbf{M} = -[\mathbf{B} \times] \mathbf{D} \quad (45)$$

where $[\mathbf{B} \times]$ is the skew symmetric matrix obtained applying the $[\cdot \times]$ operator to the magnetic field vector in body frame, measured by the magnetometer. However, it is not possible to compute \mathbf{D} by inverting Equation 45 because $[\mathbf{B} \times]$ is singular. This reflects the fact that is never possible to generate three independents components of the control torque since \mathbf{M} is always perpendicular to both \mathbf{D} and \mathbf{B} . One possible solution is to add one or more reaction wheels. It was chosen to add two reaction wheels, one along \mathbf{x}_B and one along \mathbf{y}_B in \mathcal{B} frame. This is because, as it is shown in Equation 47 and Equation 48, when only one reaction wheel is used, the matrix of the linear system becomes singular when the component of the magnetic field aligned with the reaction wheel is zero. As shown in Figure 6, all components of the magnetic field will go to zero at a certain point.

If just one reaction wheel would be used, it should be deactivated when the respective component of \mathbf{B} goes to 0. This would mean that for certain times the only actuator that could operate would be the magnetorquer. This would lead to the undeterminate problem of defining a command to the magnetorquer, as seen in Equation 33. Following the considerations just given, the command is always given in the form:

$$\mathbf{cmd} = [D_x \ D_y \ D_z \ -\dot{h}_x \ -\dot{h}_y]^T \quad (46)$$

where D_x , D_y and D_z are the dipoles to be given by the magnetic coils, \dot{h}_x and \dot{h}_y are the moments to be given by the reaction wheels.

Only one reaction wheel is used at a time, they are never used together. A logic was implemented to choose which reaction wheel to use. It consists in an if/else construct, implemented in Simulink through two enabled subsystems, which takes as condition $|B_x| \geq 10^{-5} \text{ T}$. If the condition is satisfied, the reaction wheel along x is used and the linear system reported below is solved:

$$\begin{bmatrix} 1 & B_z & -B_y \\ -B_z & 0 & B_x \\ B_y & -B_x & 0 \end{bmatrix} \begin{bmatrix} -\dot{h}_x \\ D_y \\ D_z \end{bmatrix} = \begin{bmatrix} M_x \\ M_y \\ M_z \end{bmatrix} \quad (47)$$

The command vector is assembled as indicated in Equation 46 by taking the solution Equation 47 and setting to zero D_x and \dot{h}_y . If the condition is not satisfied, the reaction wheel along y is used, the linear system to be solved is

$$\begin{bmatrix} 0 & B_z & -B_y \\ -B_z & 1 & B_x \\ B_y & -B_x & 0 \end{bmatrix} \begin{bmatrix} D_x \\ -\dot{h}_y \\ D_z \end{bmatrix} = \begin{bmatrix} M_x \\ M_y \\ M_z \end{bmatrix} \quad (48)$$

and the command vector is assembled as indicated in Equation 46 by taking the solution of Equation 48 and setting to zero D_y and \dot{h}_x . The idea behind this kind of logic was to be always able to compute the command vector. Indeed, the matrix of Equation 47 is singular when $B_x = 0 \text{ T}$ and the matrix of Equation 48 is singular when $B_y = 0 \text{ T}$. It is clear that, using this kind of logic, it is always possible to compute a command to be sent to the actuators. The assumption that was made is that, at every instant of time, at least one of B_x and B_y is non-zero. Looking at the graph in Figure 6, it can be noticed that, when B_x is zero, B_y is far from zero and vice-versa. It wasn't chosen to put the second reaction wheel along z axis because, as it is shown in the graph reported in the same figure, B_z is always around the zero value. That condition would generate a high-valued command to the reaction wheels and to the dipoles. Hence, the saturation would happen earlier.

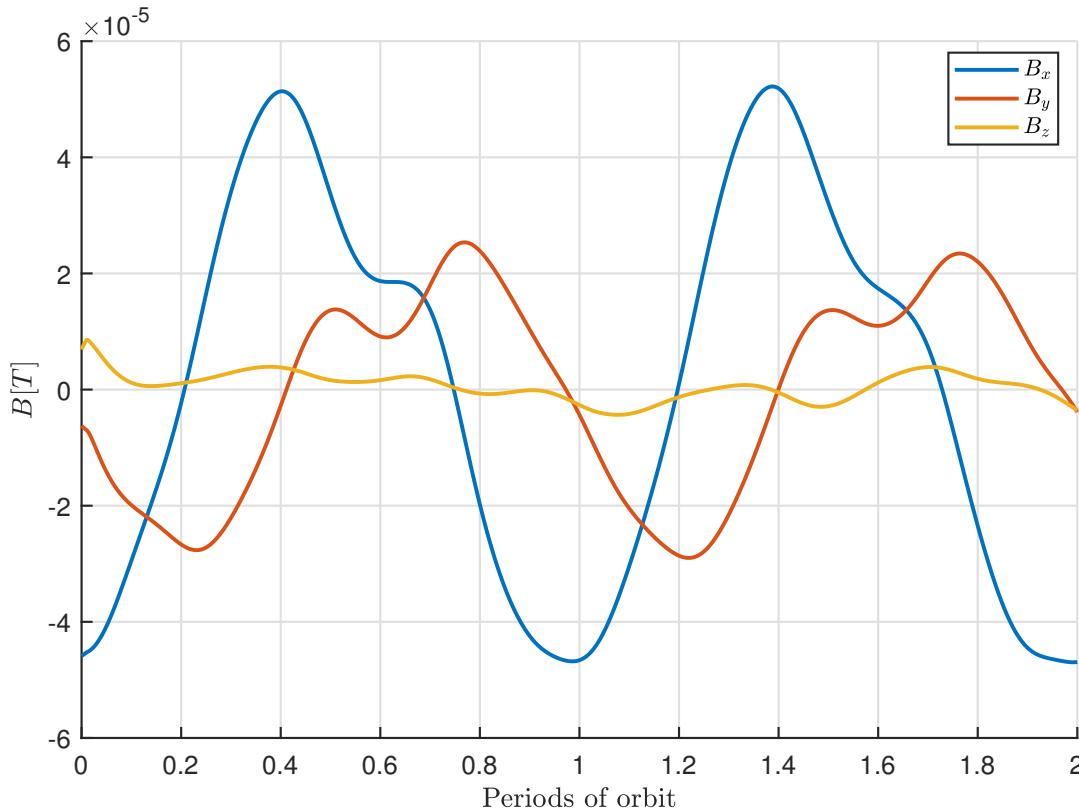


Figure 6: Magnetic Field in \mathcal{B} frame

11. Simulation results

In the present section, the results of the simulation will be presented and discussed. The simulation was executed for a period of two complete orbits in order to observe all the three main phases of the satellite's mission. It was started from random initial conditions on both angular velocity ω and Euler angles s_0 . The ω components were limited in range $-0.06 \div 0.06$ rad/s, while s components were in range $0 \div 2\pi$ rad.

Since the final mission of the satellite is Nadir pointing, particular attention is posed on the values of some physical quantities, in particular:

- ω and $\|\dot{\mathbf{B}}_m\|$ for the detumbling phase;
- α and ω_{BL} for the slew and tracking phase, where $\alpha = \frac{1}{2} (A_{BL}^T - A_{BL})^V$.

Furthermore, from the satellite operational point of view, some other physical quantities are relevant, such as the control torques \mathbf{M}_c . In addition, the angular velocities of the reaction wheels and the magnetorquers' generated dipoles will be analyzed to verify the saturation condition and the consumption power respectively.

11.1. Detumbling analysis

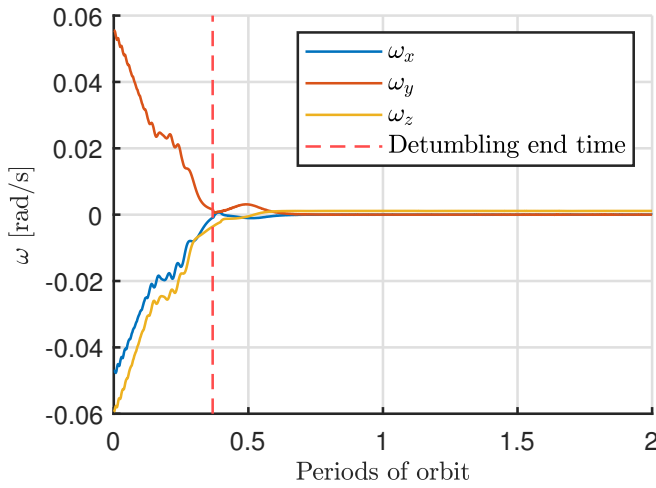


Figure 7: ω in \mathcal{B} frame

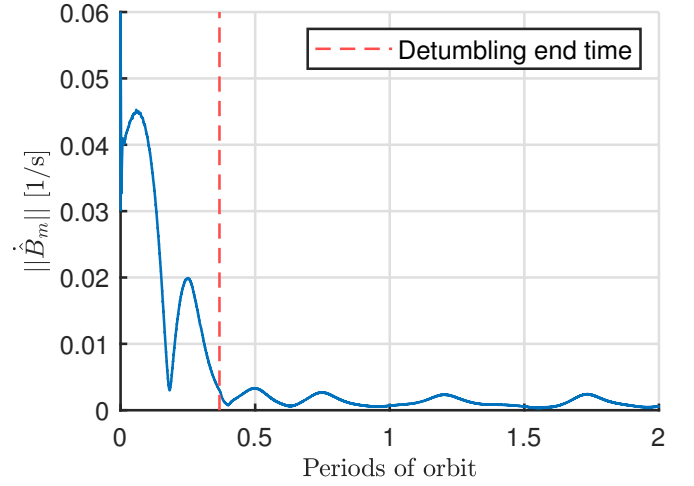
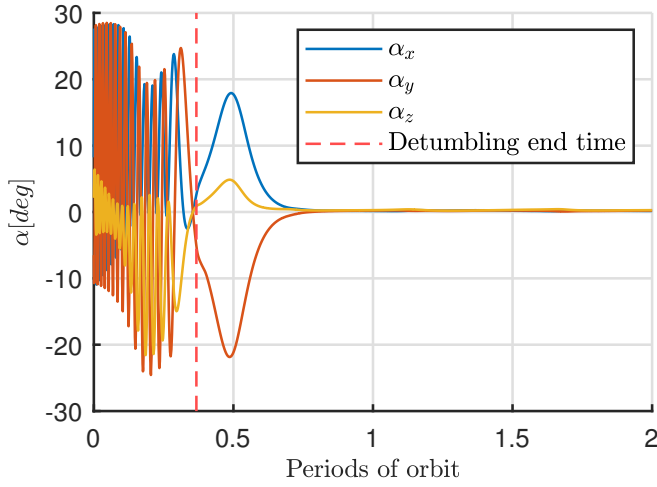
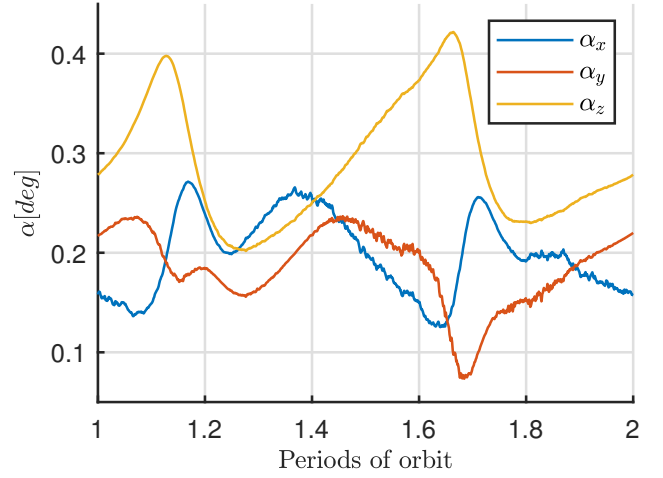
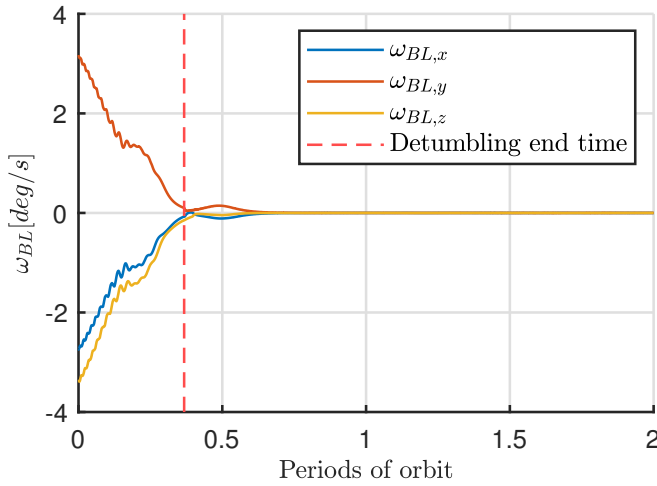
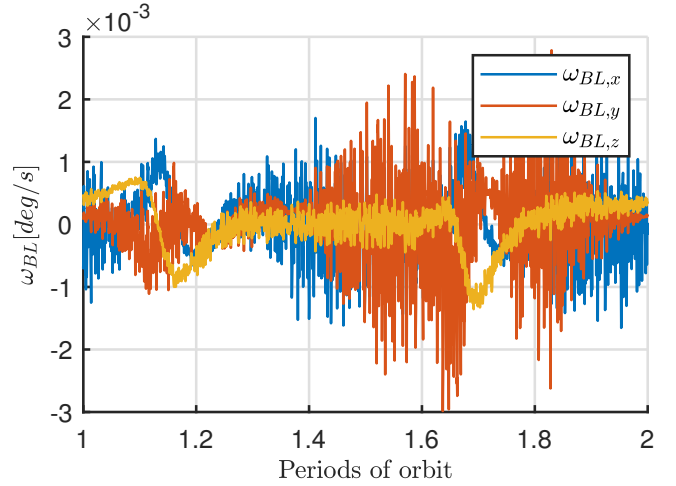


Figure 8: $\|\dot{\mathbf{B}}_m\|$ in \mathcal{B} frame

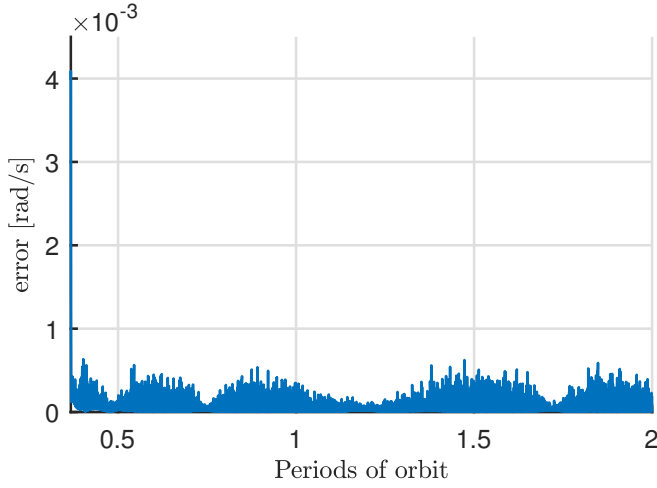
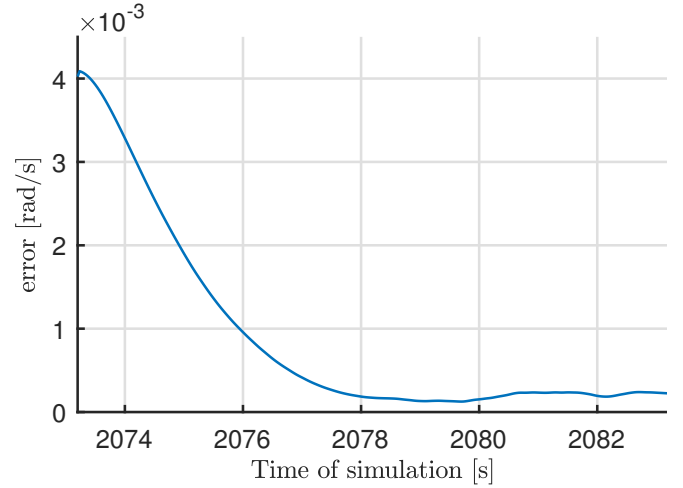
As it can be seen in Figure 7 and Figure 8, the detumbling has a duration of less than half orbit, then the slew and tracking control engages to keep the angular velocity stabilized. Note that from this particular case nothing general can be deduced, as the period and the behaviour of the detumbling phase strongly depends on the initial conditions of the satellite and also on the criteria on which the control switches to the next phase. In this simulation, this criteria is based on the evaluation of $\|\dot{\mathbf{B}}_m\|$. Looking at the graph in Figure 8, the detumbling phase ends when the condition $\|\dot{\mathbf{B}}_m\| < 0.003 \text{ s}^{-1}$ is satisfied.

11.2. Slew and tracking phase analysis

Figure 9: Attitude error α Figure 10: Zoom on α Figure 11: Angular velocity error ω_{BL} Figure 12: Zoom on ω_{BL}

In Figure 9 and Figure 11 it can be seen that, after the detumbling, there is a transient after which both attitude and angular velocity errors converge to zero in a short period of time and keep stabilized. To better evaluate the errors in the tracking phase, in Figure 10 and Figure 12 a zoom on the final phase can be appreciated. The high frequency oscillations are mainly imputable to errors introduced by sensors and actuators. Indeed, both the command to the actuators and the executed control action are affected by noise. Moreover, looking at α_z a period behaviour can be noticed. The peaks hit 0.4° value every half orbit. This can be related to the Figure 12, where the zero is crossed in corispondence of the previous peaks, and the behaviour repeats periodically as well. In addition, it can be noticed that the components of α oscillate about non-zero values, as it is present a steady-state error in the system. This could be resolved introducing an integrative term on the control.

It can be noticed from Figure 9 and Figure 11 that, at the beginning of slew manoeuvre, both attitude and angular velocity errors increase before going towards zero. This can be explained by Figure 14, in which the estimation of the angular velocity done by the alghoritm presented in subsubsection 10.2.1 is initially rough as it comes from the numerical derivation of A_{BN} .

Figure 13: $\|\omega_{estim} - \omega\|$ after detumblingFigure 14: $\|\omega_{estim} - \omega\|$ in the first 10 s after detumbling

As can be seen in Figure 13, after the error in estimated angular velocity decreases it stabilizes itself toward values close to zero.

11.3. Control action analysis

Another important perspective to consider is how the actuators behave during the simulation, in particular verifying the torque generated and the reached saturation levels. For this last point, it can be evaluated whether a desaturation algorithm becomes necessary to be implemented on the reaction wheels. For the dipoles, this analysis could be useful to dimension the energy supply (i.e. the solar panels and batteries).

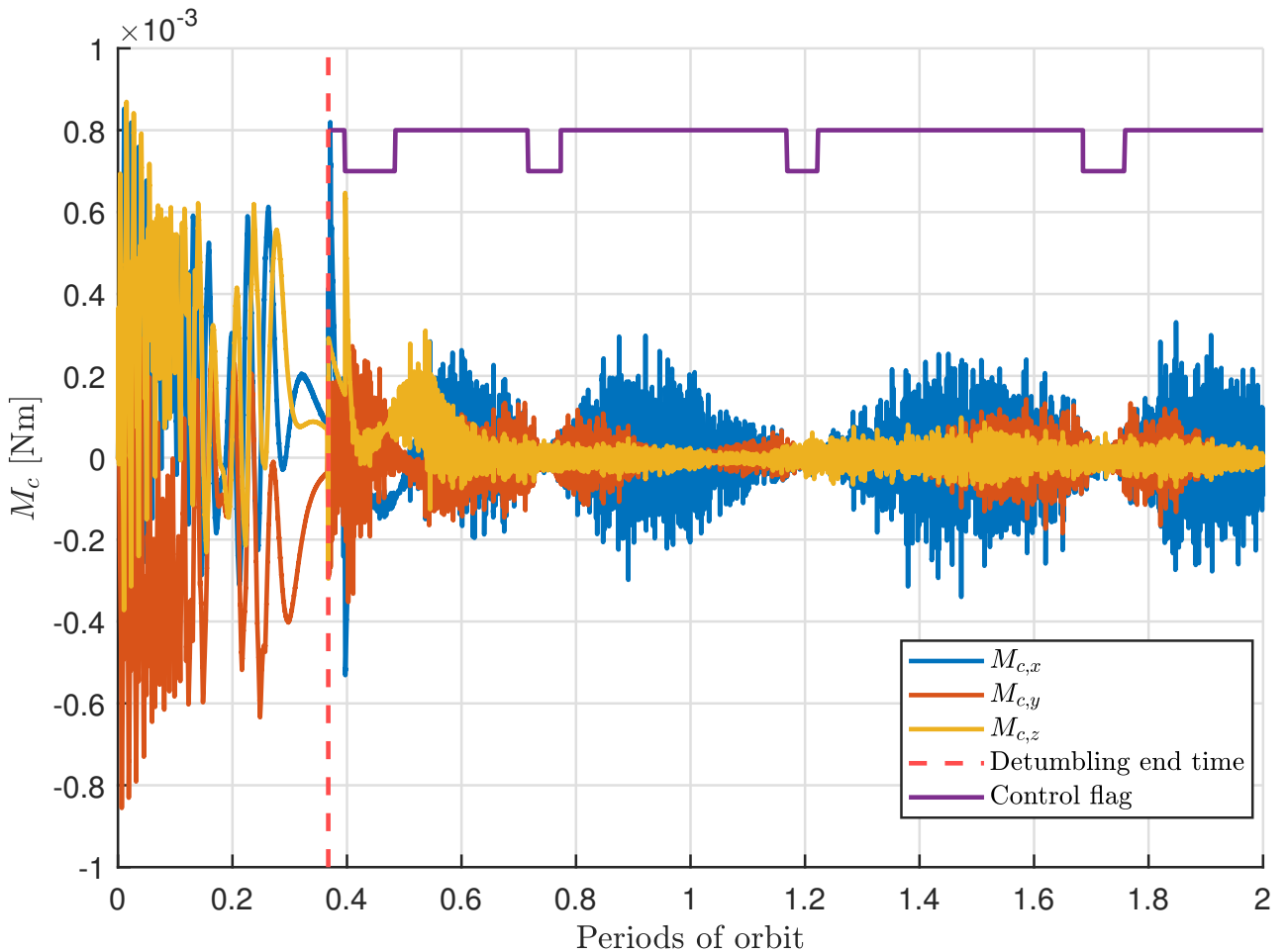


Figure 15: Actuated torque and control logic flag on reaction wheels

From Figure 15 it can be noticed that the torque is greater but much less noisy on detumbling phase than the tracking phase. Indeed, the control action during the first phase is calculated basing on the information coming only from the magnetometer, which is far more accurate than the other sensors (Table 6). Right after the detumbling phase, the slew manoeuvre presents a peak on the control torque requested. It is imputable to the bad estimation on the angular velocity on the starting phase, as seen in Figure 14.

During the tracking phase, a low-frequency harmonic can be detected in the control moment, which is most noticeable on the x component. This behaviour can be related to the activation of the reaction wheel on the same axis, as can be seen from the control flag. It can also be seen that the time of activation of the wheel on x axis is longer than that on y axis. A possible alternative to this implementation could involve a better load distribution between the reaction wheels, again taking into account the variation in the magnetic field which rules the control logic.

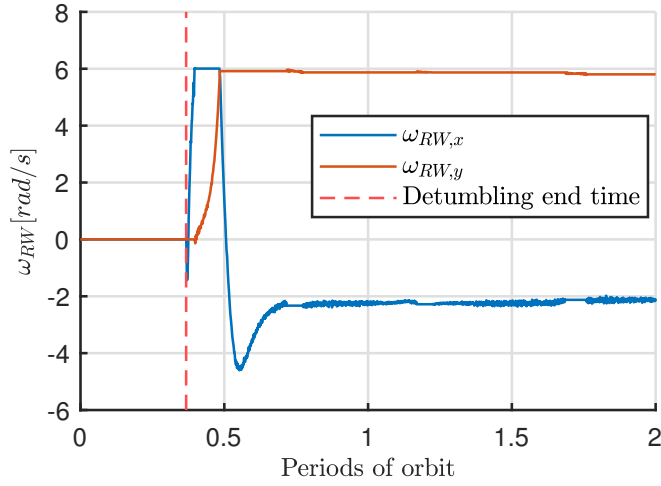


Figure 16: Angular velocities of RW

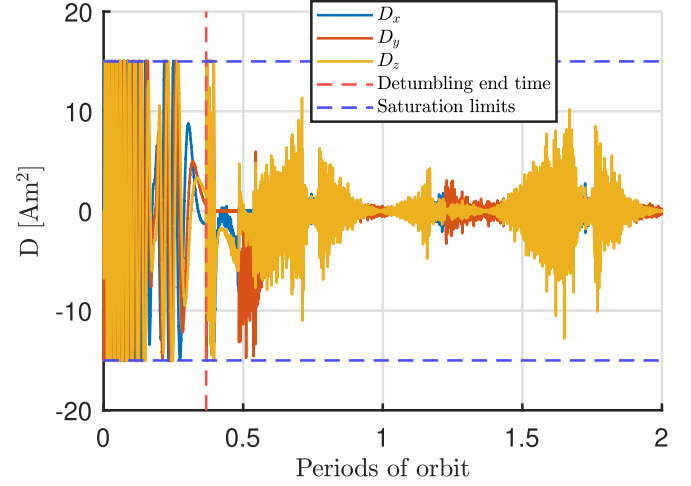


Figure 17: Dipole of magnetic coils

In Figure 16 is shown the angular velocities of the two reaction wheels. The saturation rates (Table 9) are much bigger in absolute value with respect to the values reached during the simulation. The Figure 17 shows instead the magnitude of the magnetic dipoles along the three axis. The most critical phase for the magnetorquer is surely the detumbling phase, since the control torque is relatively high (as noted in Figure 15) and magnetorquer is the only actuator used. It can be observed that the value of the dipole components saturate almost constantly. Since the dipole supplied by the magnetorquer is directly proportional to the current, the batteries must be sized in order to supply the required energy during the phase with retracted solar panels.

Bibliography

- [1] ESA. Esail maritime satellite launched. Website, 2020. Site: https://www.esa.int/Applications/Connectivity_and_Secure_Communications/ESAIL_maritime_satellite_launched.
- [2] Howard D. Curtis. *Orbital Mechanics for Engineering Students*. Elsevier, 2014.
- [3] ESA. Types of orbits. Website, 2020. Site: https://www.esa.int/Enabling_Support/Space_Transportation/Types_of_orbits.
- [4] James R. Wertz. *Spacecraft Attitude Determination And Control*. Kluwer Academic Publishers, 1978.
- [5] Meisei. Horizon sensor. Website, 2020. Site: <https://www.meisei.co.jp/english/products/space/satellite-components/p1380>.
- [6] AAC ClydeSpace. Sun sensor. Website, 2021. Site: <https://www.aac-clyde.space/what-we-do/space-products-components/adcs/ss200>.
- [7] John I. Crassidis F. Landis Markley. *Fundamentals of Spacecraft Attitude Determination and Control*. Springer, 2014.
- [8] AAC ClydeSpace. Magnetorquer. Website, 2021. Site: <https://www.aac-clyde.space/what-we-do/space-products-components/adcs/mtq800-10>.
- [9] O.C.E. Technologies. Rw40. Website, 2022. Site: <https://satsearch.co/products/oce-technology-rw40-reaction-wheel-4nms>.
- [10] Giulio Avanzini, Fabrizio Giulietti. Magnetic Detumbling of a Rigid Spacecraft. *Journal of Guidance, Control and Dynamics*, 35(4):1326–1333, 8 2012.
- [11] M. Lovera, A. Astolfi. Spacecraft attitude control using magnetic actuators. *Elsevier*, 40(4):1405–1414, 2 2004.